AGU PUBLICATIONS

JGR

Journal of Geophysical Research: Oceans

RESEARCH ARTICLE

10.1002/2014JC009894

Observations of surface waves interacting with ice using stereo imaging

Alexander J. Campbell[1], Adam J. Bechle[1], and Chin H. Wu[1]

[1]Department of Civil and Environmental Engineering, University of Wisconsin-Madison, Madison, Wisconsin, USA

Key Points:

- Stereo imaging is used to remotely measure waves interacting with ice
- Pancake and frazil ices differentially attenuate higher-frequency waves
- Brash ice causes a rapid increase in dominant wave frequency

Correspondence to:
C. H. Wu,
chinwu@engr.wisc.edu

Citation:
Campbell, A. J., A. J. Bechle, and C. H. Wu (2014), Observations of surface waves interacting with ice using stereo imaging, *J. Geophys. Res. Oceans*, *119*, 3266–3284, doi:10.1002/2014JC009894.

Received 7 FEB 2014
Accepted 12 MAY 2014
Accepted article online 19 MAY 2014
Published online 2 JUN 2014

Abstract A powerful Automated Trinocular Stereo Imaging System (ATSIS) is used to remotely measure waves interacting with three distinct ice types: brash, frazil, and pancake. ATSIS is improved with a phase-only correlation matching algorithm and parallel computation to provide high spatial and temporal resolution 3-D profiles of the water/ice surface, from which the wavelength, frequency, and energy flux are calculated. Alongshore spatial frequency distributions show that pancake and frazil ices differentially attenuate at a greater rate for higher-frequency waves, causing a decrease in mean frequency. In contrast, wave propagation through brash ice causes a rapid increase in the dominant wave frequency, which may be caused by nonlinear energy transfer to higher frequencies due to collisions between the brash ice particles. Consistent to the results in frequency, the wavelengths in pancake and frazil ices increase but decrease in brash ice. The total wave energy fluxes decrease exponentially in both pancake and frazil ice, whereas the overall energy flux remain constant in the brash ice due to thin layer thickness. The spatial energy flux distributions also reveal that wave reflection occurs at the boundary of each ice layer, with reflection coefficient decaying exponentially away from the ice interface. Reflection is the strongest at the pancake/ice-free and frazil/brash interfaces and the weakest at the brash/ice-free interface. These high resolution observations measured by ATSIS demonstrate the spatially variable nature of waves propagating through ice.

1. Introduction

Surface wave propagation through ice is a complex physical process that occurs in cold oceanic and lacustrine environments [*Squire et al*., 1995]. For a few months within a year, waves in the presence of ice can create several issues in both coastal and offshore waters [*Forbes and Taylor*, 1994]. For example, waves interacting with ice can impede navigability of ships by creating hazardous operating conditions from increased loading on the hull [*Ibrahim et al*., 2007]. Force induced on coastal structures from waves through an ice field can be magnified up to 5 times greater than that of open water waves [*Foschi et al*., 1996], resulting in structural failure [*Ibrahim et al*., 2007]. Additionally, wave action with ice along the shoreline can entrap beach sand in floating fragments of ice and transport sediments offshore [*Barnes et al*., 1994]. Overall, these problems are largely dependent on the type of ice that forms at a given location, as each ice type causes a unique modulation of wave characteristics [*Wadhams*, 2001]. Therefore, characterizing wave interaction with different ice types is crucial to improving our knowledge of how waves propagate through ice and the resulting issues associated with this phenomenon.

Three common ice types that occur in both coastal and offshore waters are frazil, pancake, and brash ice. The type of ice formed largely depends on the environmental conditions. For example, brash ice is formed by the accumulation of floating fragments made up of the wreckage of preexisting forms of ice. Therefore, owing to the formation process, the physical characteristics of the brash ice particles are highly dependent on the preexisting ice from which it was formed. In another case, if open water is supercooled and dominated by turbulence from strong winds, small ice crystals, called frazil ice, would be formed [*Wadhams*, 2001]. Frazil crystals are adhesive with each other, resulting in the formation large flocs of particles [*Ghobrial et al*., 2013]. Under wavy conditions, frazil ice flocs experience cyclical compression and freeze together to form pancake ice [*Wadhams*, 2001]. The size of pancake ice is dictated by the wave condition, in particular wavelength and amplitude [*Shen et al*., 2001, 2004]. Pancake ice is more rigid in comparison with frazil ice and is generally underlaid by frazil ice [*Shen et al*., 2004]. Owing to this formation process, the pancakes have rounded edges and jagged bottoms which can lead to significant drag on the particles [*Kohout et al*., 2011]. Previous study by *Squire et al*. [1995] showed that the various physical properties of these different ice types alter the kinematic and dynamic behavior of surface waves interacting with ice.

Several mechanisms have been proposed to describe the characteristics of waves interacting with ice based on the physical properties of ice types. The thin elastic plate model is used to describe wave propagation through a continuous unbroken ice sheet for which the flexural behavior of the ice dominates [*Wadhams*, 1986; *Fox and Squire*, 1990, 1991]; elastic ice conditions were not observed in this study. For both frazil ice and pancake ice, the cohesion between ice particles is strong, yielding the ice layer to act like a viscous fluid [*Weber*, 1987; *Keller*, 1998]. Viscous theory predicts wave energy to decay exponentially with propagation distance into the ice field, with observed energy attenuation rates on the order of 10^{-4} for lower-frequency waves ($f < 0.15$ Hz) [*Wadhams*, 2001] and 10^{-1} for higher-frequency waves ($f > 0.5$ Hz) [*Newyear and Martin*, 1997; *Wang and Shen*, 2010a]. In brash ice, the cohesion between particles is minor, and the particles are typically small relative to wavelength. Thus, the environment with brash ice is treated as a collection of point masses which exert a pressure on the water surface, known as the mass loading model [*Weitz and Keller*, 1950]. Energy attenuation due to brash ice is typically approximated by an exponential decay with propagation distance, with observed attenuation rates on the order of 10^{-4} [*Squire and Moore*, 1980; *Frankenstein et al*., 2001]. To avoid rigid classification that may inaccurately describe the inhomogeneous ice fields, viscoelastic models have been developed to treat ice as a parameterized continuum of ice types [*Wang and Shen*, 2010b, 2011, 2013; *Squire*, 2011]. While observations are crucial to validate models of wave behavior through ice [*Squire*, 2007, 2011], the availability of field data is limited.

Difficulties in the measurement of wave interaction with ice contribute to the scarcity of available data [*Squire*, 2007]. For example, capacitance wire wave gauges attain a high temporal wave time series but can be easily damaged by floating ice particles. Submerged pressure sensors avoid direct contact with the ice but converting pressure to wave height can be challenging, especially in the presence of ice at the surface [*Goodman et al*., 2010]. Wave buoys provide point measurements of wave height, frequency, and direction but are limited to a certain threshold of high-frequency waves [*Fox and Haskell*, 2001]. In addition, these discrete point measurements require an array of sensors to measure the propagation of waves interacting with ice [*Wang and Shen*, 2010a]. Nevertheless, the installation of sensors over a span of distance can be costly. Autonomous underwater vehicles mounted with acoustic Doppler current profilers can capture waves on a vast spatial scale [*Squire et al*., 2009], though vehicle surge response can contaminate the results, especially at lower frequencies [*Hayes et al*., 2007]. Satellite synthetic aperture radar imagery has been successfully used to measure waves over a large area [*Alpers et al*., 1981] and through ice fields [*Wadhams et al*., 2004]. Nevertheless, time interval between measurements is usually much larger than the wave period. Consequently techniques that provide concurrent spatial and temporal measurements are highly desired, which can be of importance to reveal the modulation of wave characteristics in the presence of ice.

In recent years, stereo imaging has emerged as an effective remote method to spatially and temporally measure surface wave characteristics. Stereo imaging uses a minimum of two images taken at different vantage points to triangulate the three-dimensional coordinates of the water surface. In the past, stereo imaging was used to measure the surface topography of waves [*Schumacher*, 1939; *Cote et al*., 1960; *Sugimori*, 1975; *Holthuijsen*, 1983; *Shemdin et al*., 1988; *Banner et al*., 1989], but data obtained from the early applications were limited owing to lengthy processing times. Contemporary improvements in computational speed and imaging hardware have led to a great deal of progress in stereo imaging measurements of water waves. For example, an Automated Trinocular Stereo Imaging System (ATSIS), developed by *Wanek and Wu* [2006], was used to measure the spatial evolution of large-scale breaking waves and small-scale capillary waves at a high frequency (10 Hz). The Wave Acquisition Stereo System, developed by *Benetazzo* [2006] and updated by *Benetazzo et al*. [2012], was employed to measure the wave dispersion relation in the presence of a current. Furthermore, *de Vries et al*. [2011] deployed a wide baseline set of cameras to measure nearshore waves over a large-scale area (1000 m^2). To improve efficiency in stereo processing, *Bechle and Wu* [2011] developed near real-time virtual wave gauge algorithm to characterize offshore breaking waves and nearshore waves interacting with coastal structures. To date stereo imaging has been proved to be a powerful tool to remotely measure surface waves. Nevertheless, stereo-imaging has not been employed to observe waves propagating through ice, as far as the authors are aware.

Table 1. Weather Conditions for Experiments and ATSIS Setup

Experimental Case	Date	Time (CST)	Ice Description	Wind Direction	Wind Speed (m/s)	Temperature (°C)	Baseline Distance (m)	Max Camera/Object Distance
1	12/5/2011	10:00 AM	No Ice	330°	4.5	−1.2	0.77	43
2	12/26/2012	11:00 AM	Pancake ice	0	5	−5	0.8437	45
3	12/19/2009	11:00 AM	Brash ice far from shore, frazil ice close to shore	350°	7	−3.5	0.91	40

In this paper, stereo imaging is employed in the field to quantify the transformation of waves propagating from an open water ice-free condition to three different types of ice: frazil, pancake, and brash ice. The frequency, wavelength, speed, and energy of waves interacting with ice are calculated and compared to the incident waves under the ice-free condition. Results show that the wave spectrum is spatially inhomogeneous through all ice types, owing to frequency-dependent attenuation rates and nonlinear energy transfers. Energy damping is found to be much greater in the frazil and pancake ices than in the brash ice. Similarly, wave reflection from the ice interfaces with frazil and pancake ices is strongest and weakest for those with brash ice. In the following, section 2 details the experimental setup and the stereo imaging method. The data analysis techniques used in the study are explained in section 3. The results of the experiment are presented in section 4 and discussed in the context of ice wave theory and modeling in section 5. Conclusions and suggestions for future work are offered in section 6.

2. Experimental Methods

2.1. Experimental Cases

Field experiments were conducted during the winter seasons in Lake Mendota, Madison, WI. Three representative cases are selected here to examine wave propagation through different types of ice. Table 1 summarizes weather conditions and types of ice for each case. Case 1 is surface waves free of ice, acting as a reference in this study. Wind direction was predominantly from the northwest and wave breaking was observed to occur sporadically over the camera coverage area. Case 2 is waves with pancake ice extending approximately 31 m into the lake (see Figure 1a). Starting from no ice at the study site, the pancake ice was formed over a 36 h time period where the lake experienced northern winds in excess of 5 m/s and temperatures below −7°C. The diameter of the pancakes close to shore was about $\o \approx 70$ cm and decreased in size closer to the open water (Figure 1b). The thickness of the pancake ices was approximately 0.5 cm. Underneath the pancake ices, there was a 25 cm thick layer of small frazil ice particles with diameter of $\o = 1$ cm (Figure 1c). Case 3 is waves with mixed ices extending 30 m into the lake (Figure 1d). The first 12 m of the ice field was dominated by brash ice followed by an 18 m length of the frazil ice close to the shore. Starting from no ice at the study site, low winds and temperatures below −10°C caused a solid ice sheet to form in a bay to the west of the study side. After 2 days, temperatures below −4°C and winds from the northeast in excess of 4.5 m/s caused frazil ice to form at the study site and the solid ice sheet in the bay to fracture from wave induced loading, creating brash ice particles. On the following day winds shifted to the north-northwest and generated longshore currents which transported the brash ice from the bay to the study side offshore of the frazil ice. Owing to the formation processes, the brash ice particles were rigid with smooth top and bottom surfaces and defined angular edges (Figure 1e). Diameters of the particles were $\o \approx 40$ cm and with thickness of $\approx$4 cm. Audible collisions along with smooth rigid surfaces indicate that cohesion between particles was small. Shoreward of the brash ice, there was an 18 m length of the frazil ice with cohesive flocs with a layer thickness of approximately 30 cm (Figure 1f). The frazil particles were smaller and more cohesive than those underlying the pancake ice in Case 2.

2.2. Stereo Imaging Measurements

2.2.1. Acquisition

Figure 2 shows the Automated Trinocular Stereo Imaging System (ATSIS), developed by *Wanek and Wu* [2006]. ATSIS consists of three progressive scanline IEEE-1394 cameras (Basler A602-f), capable of recording 100 frames per second at their full resolution of 640 × 480 pixels. The cameras were affixed with a 16 mm lens with a view of 22° × 16° in the horizontal and vertical, respectively. Each camera was fastened to an adjustable pan/tilt tripod head mounted to a single aluminum bar with a baseline distance between

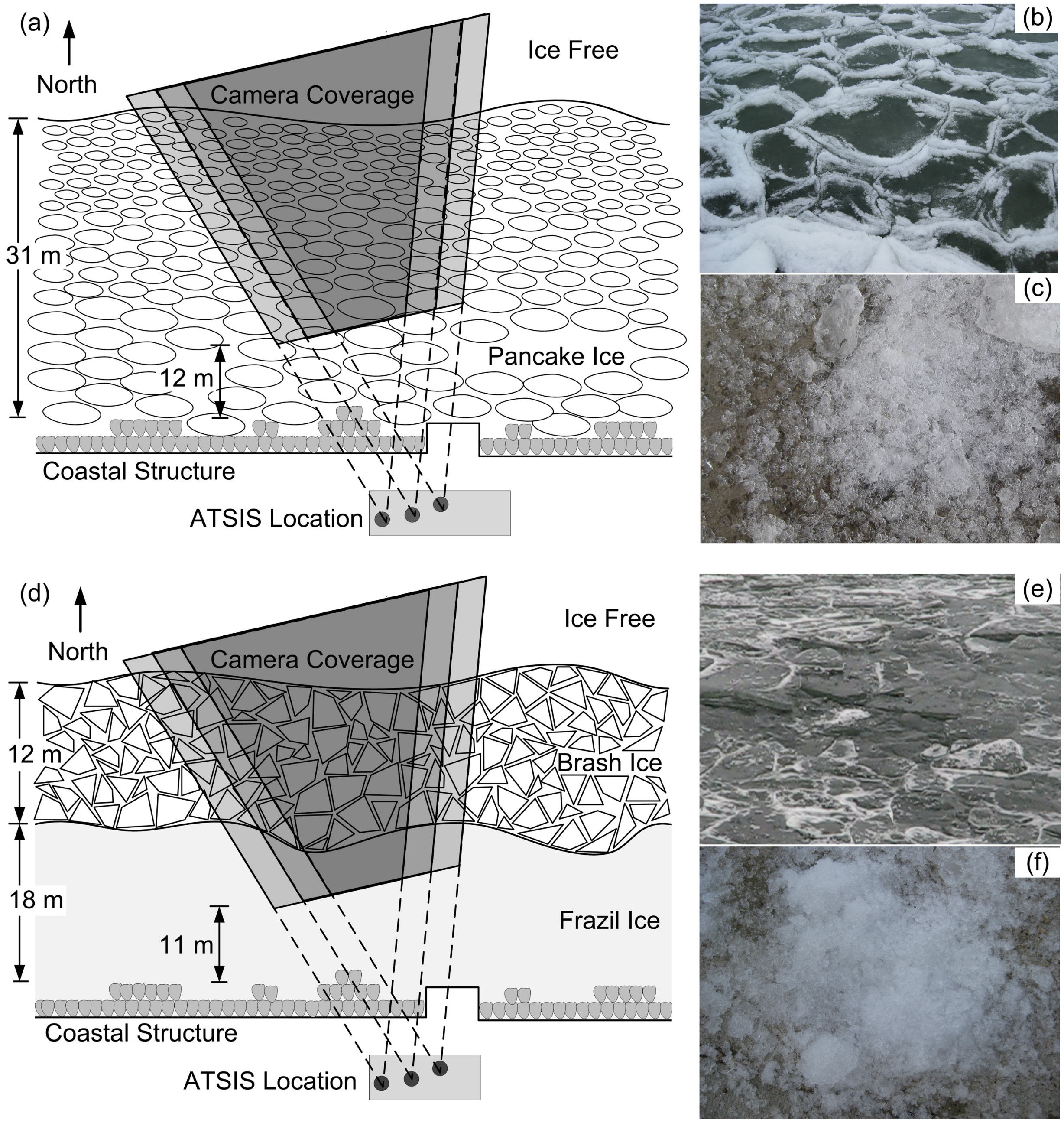

Figure 1. Schematic of the experimental setup for (a) Case 2 and (d) Case 3 with photos of (b) pancake ice and (c) underlying frazil ice crystals in Case 2; (e) brash ice and (f) frazil ice in Case 3.

adjacent cameras of 1 m and a baseline between the two end cameras of 2 m. The bar was attached to a portable tripod to facilitate field setup. The cameras were synchronized using a hand-held TTL signal generator, and the images were recorded directly to a hard drive on a laptop computer. ATSIS was setup on top of a platform 5 m above the water surface and 4 m away from the coastline (Figures 1a and 1d). The stereo cameras covered an approximate area of 200 m^2 for each of the three cases. Table 1 summarizes the ATSIS setup and configuration for each experimental case.

2.2.2. Calibration

A two-step interior-exterior calibration procedure is performed on each camera. Interior calibration rectifies the digital images to remove radial lens distortion [*Holland et al.*, 1997]. Exterior calibration determines the geometric relationship between the three cameras and the coordinate system. In typical stereo applications,

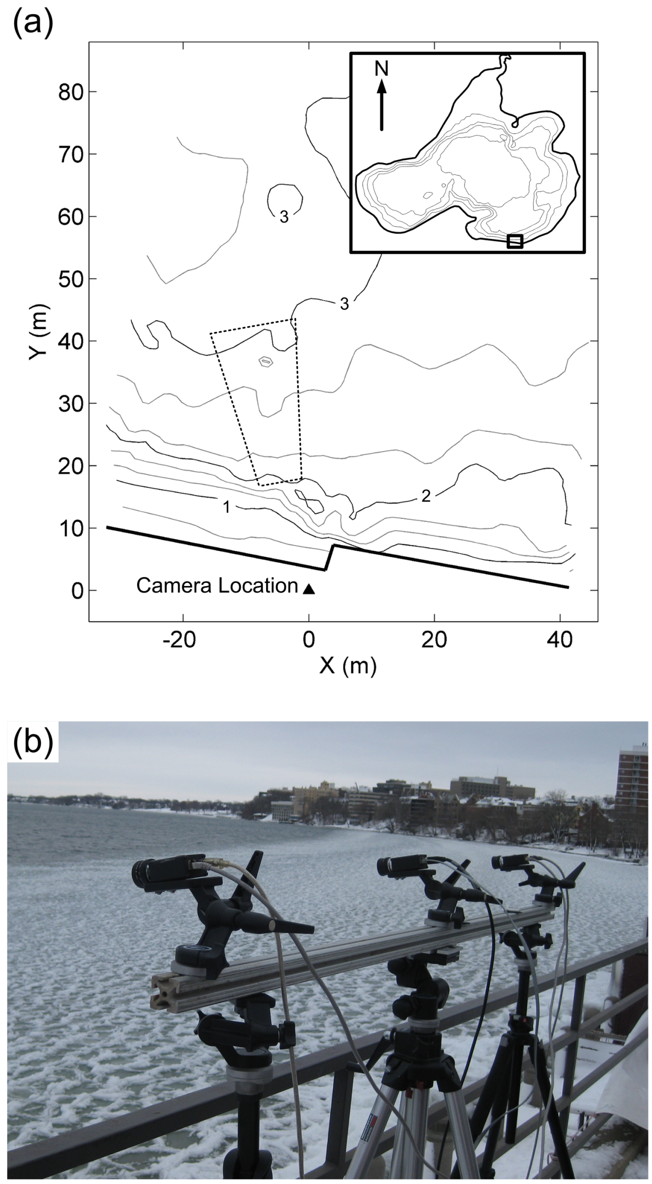

Figure 2. (a) Study site and bathymetry of Lake Mendota, Madison, WI. The dotted line indicates the camera coverage region. (b) Image acquisition in the field using the Automated Trinocular Stereo Imaging System (ATSIS).

exterior calibration utilizes ground control points to calibrate the cameras [*Holland et al.*, 1997] though for measurements over water, placing control points on the wavy water surface for a large area can be challenging [*de Vries et al.*, 2011]. This is especially difficult for an ice and wave environment. Therefore, we employ an in-house calibration method developed by *Wanek and Wu* [2006]. First, ATSIS is setup in the field and the aluminum bar is leveled. Each camera is adjusted with the pan/tilt head to view the desired scene, and the camera is then locked in place. After field measurements, the ATSIS was brought back in the lab and set up in a leveled position. The in-house calibration is performed using a precise three-dimensional calibration grid frame [*Wanek and Wu*, 2006] to register the orientation of each camera.

2.2.3. Stereo Matching

Three-dimensional positions of the water surface are determined from the location of the corresponding point in each image using the principle of triangulation. For detailed theory behind stereo imaging principles, readers can refer to *Wolf and DeWitt* [2000]. The process of locating the corresponding point in each image is known as stereo matching [*Brown*, 1992]. In this paper, a two-step area-based matching algorithm is used to achieve subpixel level accuracy; details of the stereo matching can be found in *Wanek and Wu* [2006]. Different from previous matching algorithms based upon normalized cross correlation (NCC), we employ a phase-only correlation (POC) algorithm. The basic concept of POC is built upon the Fourier shift property, which states that a shift in the spatial domain between two signals is transformed in the Fourier domain as a linear phase difference [*Foroosh et al.*, 2002]. The advantage of POC over traditional NCC-based algorithms [*Wanek and Wu*, 2006] is the reduction of computational cost [*Foroosh et al.*, 2002]. For example, to match a single pixel, NCC algorithms require multiple NCC computations along an epipolar line whereas the POC algorithm requires only one calculation for a single pixel. In this study the POC algorithm is found to reduce computational time by 25% in comparison with traditional NCC algorithms. To achieve subpixel matching accuracy in the second step, we employ the nonlinear affine relationship in *Wanek and Wu* [2006]. The subpixel matching greatly improves the accuracy of the stereo reconstruction by removing the quantization constraint of digital images [*Jähne et al.*, 1994; *Wanek and Wu*, 2006]. This two-step stereo matching algorithm is extended to three cameras by designating one image, typically the center camera, and performing matching on both the remaining cameras independently. Parallel computing technology is employed to efficiently process stereo images.

3. Data Analysis

3.1. Reflection Removal

Incident wave can be obscured by partially standing waves caused by wave reflection. For all cases in this study, reflected waves were present in varying degrees of intensity owing to the proximity of the field site to impermeable rock-mounted coastal structures with a submerged depth of ≈0.35 m (Figures 1a and 1d). We remove reflected waves using the method developed by *Frigaard and Brorsen* [1995] and *Baldock and Simmonds* [1999]. The concept of separating incident and reflected waves is to phase-shift two collocated time series (obtained from the 2-D surface profiles) so that the incident component of the wave signals is in phase and the reflected component of the signals is in mutually opposite phase. The sum of the two shifted signals is proportional to and in phase with the incident waves. To prevent aliasing of high-frequency waves, a band pass filter with a pass band from 0.4 to 0.6 Hz centered on the dominant frequency of the wave spectra is applied to each time series. Following the guidelines of *Frigaard and Brorsen* [1995], we set gage separation to be 1 m to minimize errors for the given frequency band. The resulting reflection removed wave surfaces are used to calculate mean frequency, average wavelength, and wave group velocity. Wave energy is estimated using the raw wave surface profiles to include the influence of the reflected waves.

3.2. Wavelet Analysis

To calculate the spectral content of the waves in both space and time, wavelet analysis is used in this paper. Wavelets are chosen, instead of the conventional Fourier analysis, due to its capability of resolving spatial or temporal wave modulation caused by ice. For all cases, analysis with a three parameters Morlet mother wavelet is performed on the water level time series at each distinct location of the cross-shore direction, defined as the *Y* axis. The nonstationary wavelet spectrum at each cross-shore location is then averaged over the entire time series to yield a spatially distributed frequency spectrum over a cross-shore transect. Furthermore, the mean frequency, calculated at each location along the *Y* axis as the centroid of the power spectrum [*Hayes et al*., 2007], is

$$f_{mean}=\int fE(f)/\int E(f)df, \tag{1}$$

where $E(f)$ is the value of the power spectrum at a given frequency f.

Wavelength modulation throughout the ice is characterized using wavelet power spectra over the 2-D cross-shore spatial wave profile. The wavelet spectrum is calculated at each time step and temporally averaged over the observation time, i.e., 3 min, to ensure a steady state wavelength spectrum at each spatial location is reached. The mean wavelength, $\bar{L}$, is taken as the centroid of the wavelength spectrum at each cross-shore spatial location along the *Y* axis, calculated by

$$\bar{L}=\frac{\int L*E(L)dL}{\int E(L)dL}, \tag{2}$$

where L is the wavelength and $E(L)$ is the power spectrum at a given wavelength L.

3.3. Wave Group Velocity

A correlation-based approach to minimize the influence of both user error and irregular waves during manual wave tracking is used to estimate wave group velocity. Specifically, the group velocity is calculated from the time delay in wave packet arrivals at two collocated "wave gauges" spaced a set distance apart. A 3 min surface displacement time series is obtained using a virtual gauge technique by *Bechle and Wu* [2011]. The separation distance between gauges, 1 m in this paper, divided by the calculated time delay gives the group velocity between the two gauges. A 1-D cross correlation is performed between the two signals, where the resulting peak correlation value corresponds to the average time delay between the signals. Prior to correlation, reflected waves are removed from each time series in a procedure described in section 3.1, as partially standing waves can interfere with the ability of the correlation method to properly identify the shoreward propagating waves. We also apply a Hamming window to each time series to reduce contamination of edge effects. This process is repeated for each spatial location in the cross-shore Y direction, providing a spatial distribution of group velocity in the cross-shore Y direction.

3.4. Energy Flux

The energy flux is calculated by

$$Flux(f)=E(f)C_g(f), \tag{3}$$

where E and C_g are the total wave energy and the group speed, respectively. Assuming an equal partition of potential and kinetic energy of waves in ice [*Wadhams et al.*, 1986], total wave energy is estimated by

$$E_{total}=\rho g\overline{\underline{\eta}^2}, \tag{4}$$

where η_{J}^{2J} is the standard deviation of the displacement time series η [*Holthuijsen*, 2007], ρ is the density of water, and g is acceleration due to gravity. To determine the energy flux of individual frequency bands, a band-pass filter is applied to the displacement time series to isolate the desired range of frequencies for both total energy and group velocity calculations. We will examine the effects of ices on spatially varying group velocity and energy flux.

3.5. Reflection

Sources of reflection in this study include coastal wall structure and the interface between ice-free waves and each type of ice layer. Reflection coefficient, K, the ratio of reflected and incident wave height, is estimated by

$$K=\sqrt{\int_{f_{\min}}^{f_{\max}} E_R(f)df \Big/ \int_{f_{\min}}^{f_{\max}} E_I(f)df}, \tag{5}$$

where f_{min} and f_{max} are the minimum and maximum frequency of the wave energy. For all three study cases, we use $f_{min}=0.4$ Hz and $f_{max}=0.6$ Hz; E_R and E_I are the reflected and incident wave energies, respectively [*Frigaard et al.*, 1997]. The reflected and incident wave energies are calculated at each cross-shore location in Y with a spatial resolution of 0.2 m using the incident and reflected wave separation method described in section 3.2, where the energy for both the reflected and incident waves are calculated using equation (4).

4. Results

4.1. Water Surface Displacement

Time series of three-dimensional (3-D) water surface displacements obtained from ATSIS can be used to characterize the temporal and spatial characteristics of waves interacting with ice. The vertical resolution of surface displacement is 0.5 cm based upon the error analysis of *Benetazzo* [2006] and the subpixel matching algorithm of *Wanek and Wu* [2006]. Figures 3a–3c and 4a–4c show snapshots of the 3-D water surface displacements with a 0.03 m spatial resolution and a time interval of 0.5 s for Case 2: pancake ice, and Case 3: brash/frazil ice, respectively. For better visualization, the vertical (Z) scale is accentuated. The grayscale values of the water surface are retrieved from the corresponding image coordinates on the water surface. Surface elevation contour plots corresponding to the 3-D water surfaces are shown in Figures 3d–3f and 4d–4f, which depict the temporal evolution of wave crests and troughs interacting with ice.

Significant wave modulation due to the pancake and frazil/brash ice conditions is observed and discussed here. For Case 2: pancake ice, Figure 3 shows that the wave amplitudes within the pancake ice region, e.g., $Y<36$ m, are considerably smaller than those in the ice-free region ($Y>36$ m). As waves propagate through the pancake

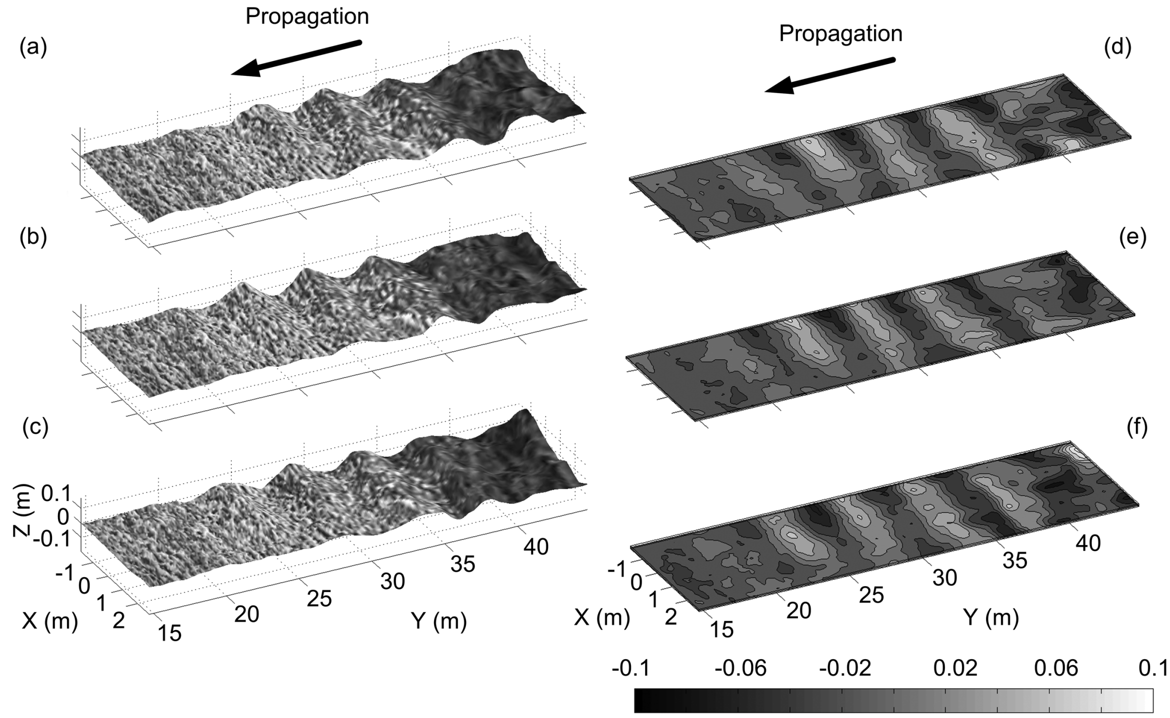

Figure 3. Processed 3-D water surface displacement profiles for pancake ice in Case 2 at (a) t = 0 s, (b) t = 0.5 s, and (c) t = 1 s with their corresponding surface elevation contours shown in Figures 3d–3f.

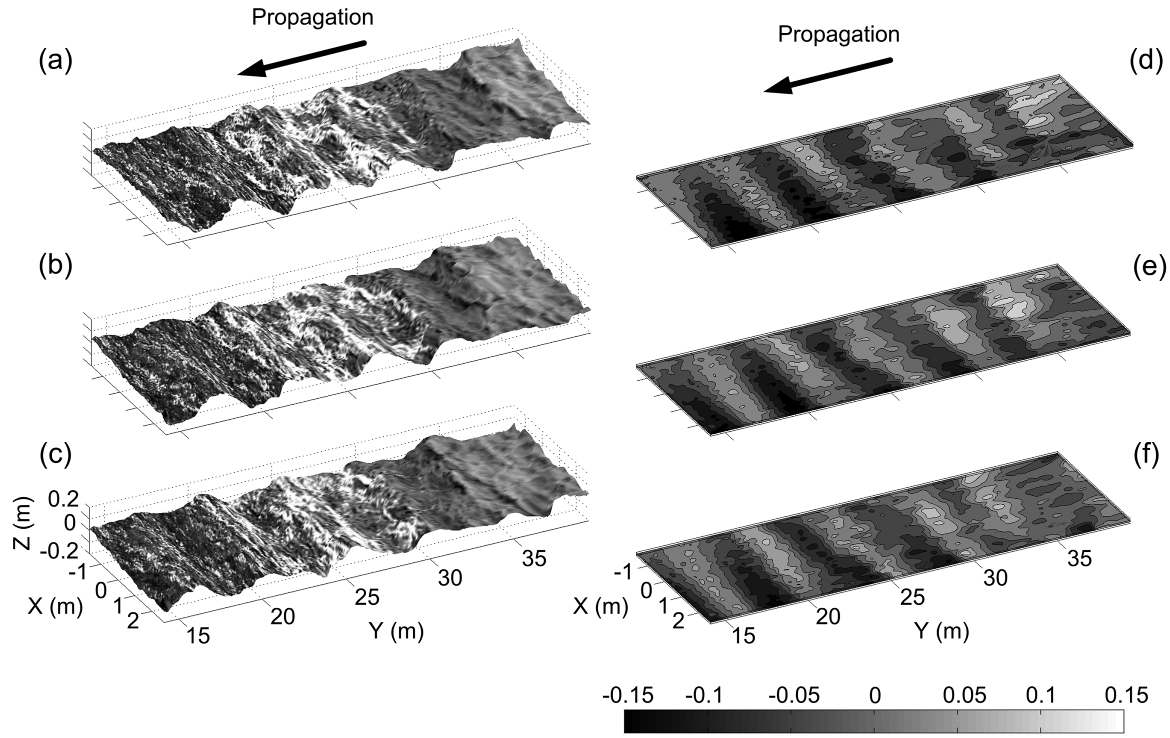

F7

Figure 4. Same as Figure 7 except for frazil and brash ice in Case 3.

ice field, short-crested waves in the open water transform to more uniform and longer crested profiles. After propagation through the ice, the wavelengths also elongate. This may indicate pancake ice attenuates high-frequency waves faster than lower-frequency waves, which is further discussed in section 4.5. For Case 3: brash/frazil ice, Figure 4 shows that wave geometry in both the brash ice (26 m $< Y <$ 35 m) and frazil ice ($Y <$ 26 m) is altered. In brash ice, wavelength shortens, causing the waves to steepen from $ak = 0.08$ at the ice free-brash interface ($Y = 35$ m) to $ak = 0.12$ near the shoreward boundary of the brash ice ($Y = 28$ m). The increase in steepness may be explained by possible nonlinear energy transfers caused by scattering induced by wave-ice interactions [*Masson and LeBlond*, 1989; *Meylan and Squire*, 1996] or collisions among ice particles [*Frankenstein et al.*, 2001] which transfer energy from lower to higher frequencies, discussed further in section 4.5. Once the waves reach the frazil ice, higher-frequency waves attenuate faster than the lower frequency content, evidenced by the more uniform and elongated crests when compared to the brash ice.

In all cases, the waves travel predominately along the shoreward direction of the negative Y axis, with crests aligned with the X axis, signifying that wave heading is not altered by the ice. To confirm this observation, the directional spectrum for each case is calculated. An array of virtual wave gauges in an approach similar to *Bechle and Wu* [2011] is employed. All cases exhibit a unimodal directional spectrum dominated by a shoreward propagation direction (results not shown for brevity). Owing to this unidirectionality, further analysis and measurements in section 4 are facilitated using 2-D wave profiles in time created by taking a section cut of the 3-D data sets along the Y axis. In addition, as waves propagate from one media to another, i.e., an ice-free region to a region covered with ice, the interface between the two regions is expected to reflect wave energy [*Weitz and Keller*, 1950]. We will discuss this further in section 4.5.3.

4.2. Wavelength

Figure 5 shows the spatial variation of wavelength along the cross-shore direction, calculated using the wavelet analysis described in section 3.1. Figures 5a–5c on the first column illustrate the wavelet power spectrum averaged over the entire time series for Cases 1, 2, and 3, respectively. Figures 5d–5f on the second column depict the wavelength spectral profiles along the section cuts indicated in Figures 5a–5c, respectively. The mean wavelength at each cross-shore spatial location along the Y axis, calculated using equation (3), is shown in Figures 5g–5i on the third column. For no ice in Case 1, the wavelet power spectrum (Figure 5a) is unimodal with the peak wavelength decreasing slightly toward the shore. The wavelength change is quantified from the spectral profiles (Figure 5d), the peak wavelength decreases from $L = 6.11$ m at $Y = 32$ m to $L = 5.95$ m at $Y = 22$ m, a 0.26% decrease per meter shoreward. Likewise, mean wavelength (Figure 5g) decreases slightly from $L^{J} = 5.93$ m at $Y = 32$ m to $L^{J} = 5.83$ m at $Y = 22$ m, equivalent to a 0.17% decrease per meter of shoreward propagation.

For pancake ice in Case 2, the wavelength power spectrum (Figure 5b) is unimodal in the ice-free region ($Y > 36$ m) but becomes bimodal deep in the pancake ice ($Y < 36$ m). The spectral profiles in Figure 5e illustrate the unimodal wavelength spectrum at the shoreward limit of the ice-free region ($Y = 36$ m) with a peak wavelength of $L = 5.27$ m. At approximately, one wavelength into the pancake ice ($Y = 30$ m), the spectral profile is attenuated differentially with respect to wavelength, where waves of shorter wavelength (L $<$ 6 m) attenuate more than those of longer wavelengths ($Y > 6$ m). The differential attenuation persists deeper into the pancake ice ($Y = 25$ m) and the spectral profile becomes clearly bimodal, with peaks at $L = 4.83$ m and $L = 7.38$ m; at this location, the peak wavelength ($L \approx 5$ m) has decreased 0.76% per meter of shoreward propagation from edge of the pancake ice. Overall, while propagating through 11 m of pancake ice ($Y = 36$ m to $Y = 25$ m), the signal strength of the shorter waves ($L \approx 5$ m) decreases by 40% while the longer waves ($L \approx 7.4$ m) only decrease in signal strength by 30%, owing to differential attenuation. The differential attenuation of short waves causes an increase in the mean wavelength of the wave field (Figure 5h), which increases from $L^{J} = 5.88$ m at $Y = 36$ m at ice-free/pancake boundary to $L^{J} = 6.01$ m at $Y = 22$ m in the pancake ice, representing a 0.22% wavelength increase per meter. Thus, while the peak wavelength decreases in pancake ice, differential attenuation yields an increase in the mean wavelength for the wave field.

For the brash/frazil ice in Case 3, the wavelength power spectrum is unimodal (Figure 5c), with the peak wavelength band narrowing in the frazil ice. From the spectral profiles (Figure 5f), the peak wavelength is $L = 5.15$ m in the in the ice-free region ($Y = 34$ m). Through the brash ice, peak wavelength downshifts to $L = 4.95$ m ($Y = 26$ m) in the brash ice, a wavelength reduction of 0.48% per meter of shoreward propagation through brash ice. As waves leave the brash ice and enter the frazil ice, the wavelength spectrum

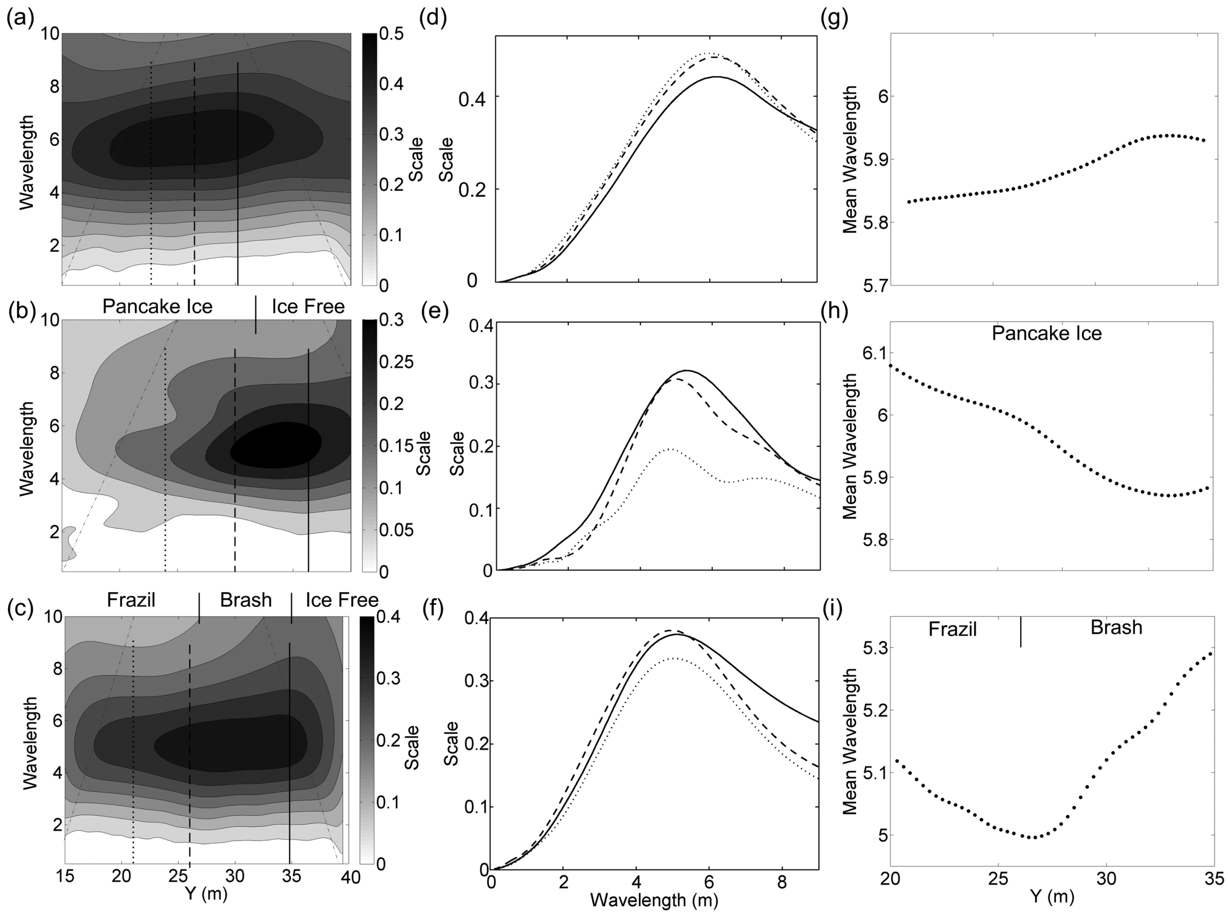

Figure 5. Wavelength power spectrum for (a) Case 1, (b) Case 2, and (c) Case 3, with the cone of influence plotted as a dash-dotted line. The solid, dashed, and dotted lines in Figures 5d–5f represent the sections cuts in Figures 5a–5c. The mean wavelength along the cross-shore Y direction corresponding to Figures 5a–5c is plotted in Figures 5g and 5h.

upshifts with a peak wavelength of $L = 5.05$ m at $Y = 22$ m, a wavelength increase of 0.51% per meter of shoreward propagation. The mean wavelength (Figure 5i) illustrates a similar trend, with a decrease in mean wavelength of 0.75% per meter shoreward brash ice and an increase of 0.37% per meter shoreward in frazil ice. The characteristics of wavelength decrease in brash ice and increase in frazil ice suggests that relative energy content of short waves increases in brash ice and decreases in frazil ice.

4.3. Group Velocity

Spatial variation of wave group velocity overall does not vary significantly as waves propagate shoreward. The group velocity remains relatively constant (2.81 m/s; $\sigma = 0.011$ m/s) for the Case 1: no ice. For Case 2: pancake ice, the group velocity increases from 3.00 m/s in the ice-free region ($Y = 36$ m) to 3.30 m/s deep in the pancake ice ($Y = 15$ m), equivalent to 0.44% increase in speed per meter. For Case 3: brash/frazil ice, waves begin with an average group velocity of 2.95 m/s in the ice-free region ($Y = 37.2$ m), decrease to 2.80 m/s in the brash ice ($Y = 27.2$ m), and then increases to 2.89 m/s in the frazil ice ($Y = 15.0$m). This change is equivalent to 0.51% decrease in group velocity per meter in brash ice and a 0.18% increase per meter in the frazil ice. Overall, the group velocity changes in Case 2 and Case 3 are consistent with those from the observed changes in wavelength.

4.4. Frequency Evolution

The spatial evolution of wave frequency using the wavelet analysis described in section 3.1 is shown in Figure 6. For no-ice in Case 1, Figure 6a shows that the waves with a dominant frequency of 0.54 Hz throughout propagate shoreward, though the spectrum contains regions of localized high and low energy. These energy minima and maxima are quasi-nodes and quasi-antinodes, caused by the partial reflection of waves

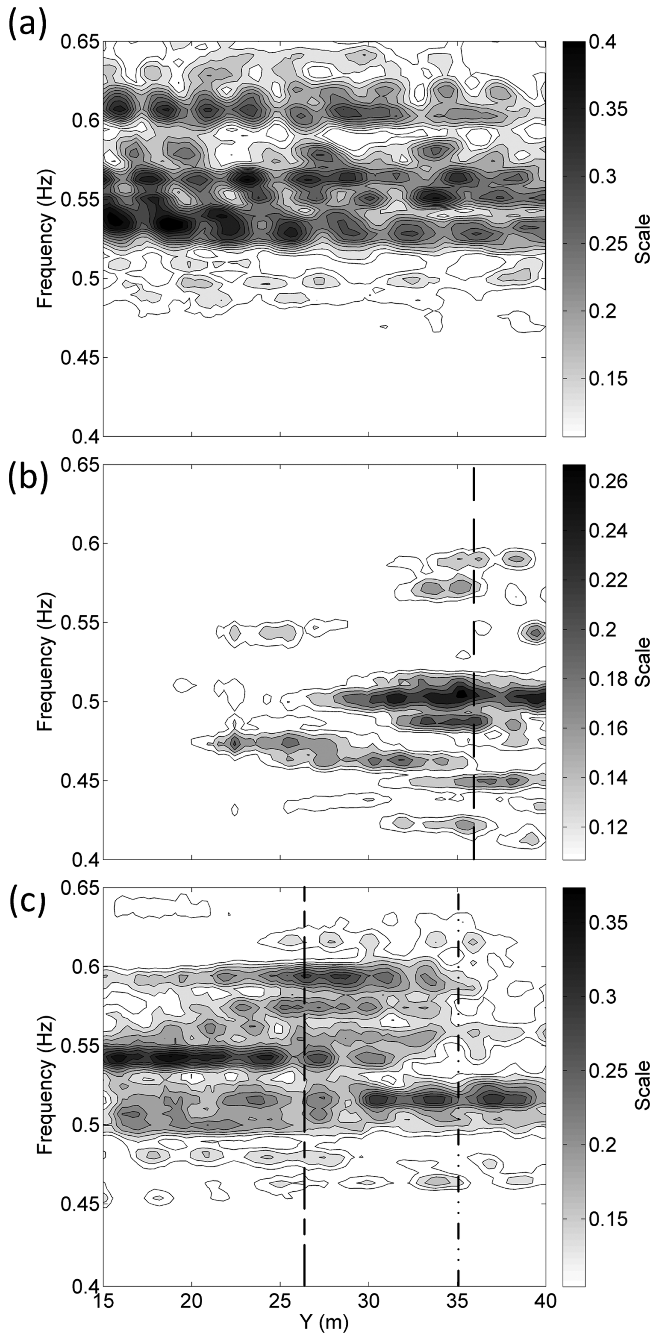

Figure 6. Frequency spectrum evolution along the cross-shore *Y* direction for (a) Case 1, (b) Case 2, and (c) Case 3. The interface between the pancake ice and ice-free region in Figure 6b is denoted by a dashed line. In Figure 6c, the interface of the brash and ice-free region is denoted by the dash-dotted; and the interface between frazil and brash ice is denoted by the long-short dashed line.

off the coastal structure. The observed spacing between the quasi-nodes and quasi-antinodes at the dominant frequency is 1.55 m, approximately close to the theoretical spacing for $f = 0.54$ Hz equal to 1.36 m, or one-quarter of the wavelength based upon deep water theory [*Dean and Dalrymple*, 1991]. Figure 7 shows the mean frequency f_{mean}, calculated using equation (1), along the cross-shore direction with a spatial resolution of 0.3 m. The mean frequency of the no-ice case, denoted as light gray circles, is relatively constant at 0.54 Hz with a small standard variation ($\sigma = 0.0028$ Hz).

For pancake ice in Case 2, the frequency content is not constant in space, as seen in Figure 6b. Specifically, the dominant frequency of 0.51 Hz in the ice-free condition ($Y > 36$m) abruptly attenuates in pancake ice ($Y < 36$m) whereas the lower-frequency waves of 0.45 Hz with slightly increasing in frequency to 0.47 Hz persist deeper into the pancake ice field. This is highlighted in the mean frequency plot in Figure 7, where the mean frequency is spatially constant at 0.50 Hz in the ice-free condition ($Y > 36$ m; medium gray circles) and steadily decreases throughout the pancake ice ($Y < 36$ m; medium gray diamonds) down to a frequency of 0.47 Hz deep in the pancake ice field ($Y = 15$ m). This decreasing frequency is attributed to the differential attenuation of wave frequencies, which will be further discussed in section 4.5.2. Similar to those seen in Case 1: no-ice (Figure 6a), the strong presence of quasi-nodes and quasi-antinodes appears in ice-free region ($Y > 36$ m), suggesting that some wave energy is reflected from the ice interface of the pancake ice [*Zhao and Shen*, 2013]. Inside the pancake ice field ($Y < 36$ m), there are weak quasi-nodes and quasi-antinodes, caused by reflected waves from the coastal structure. The magnitudes of the quasi-nodes and quasi-antinodes within the ice is much smaller than those in the ice-free region because reflected waves decay more significantly as they propagate away from the reflecting medium through the attenuating ice field than through the

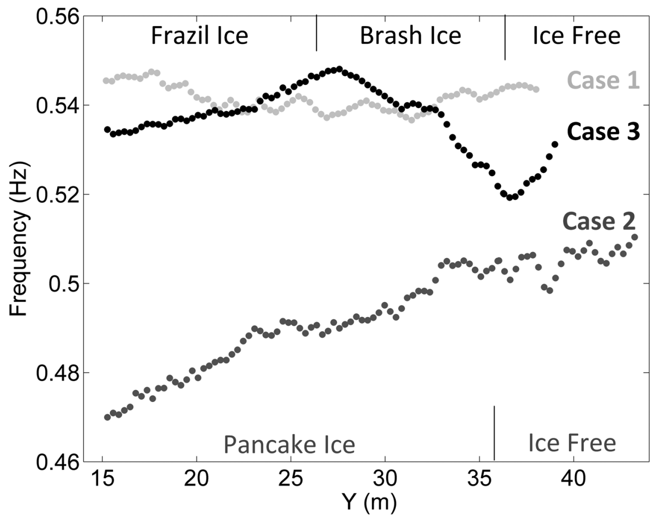

Figure 7. Mean frequency evolution along the cross-shore *Y* direction for Case 1 (●), Case 2 (●), and Case 3 (●).

ice-free region. Further discussion of reflection from both the ice edge and coastal structure will be in section 4.5.3.

For brash/frazil ice in Case 3, the spatial evolution of frequency is characterized by an increasing frequency in brash ice (26 m $< Y <$ 35 m) and a subsequent decrease in the frazil ice ($Y <$ 26 m), as seen in Figure 6c. The dominant frequency is 0.51 Hz in the ice-free region, 0.59 Hz in the brash ice region, and 0.55 Hz in the frazil ice region. The mean frequency of the brash/frazil ice, shown as dark circles in Figure 7, exhibits the spatial pattern of increasing mean frequency in brash ice and decreasing mean frequency in frazil ice. The increase in energy for higher-frequency waves in the brash ice suggests a potential nonlinear energy transfer between the ice-free into the brash ice field. Since the cohesion between brash ice particles is minor, waves interacting with ice particles may create high-frequency wave scattering [*Frankenstein et al*., 2001]. For the frazil ice, the downshift in dominant frequency is similar that in pancake ice, likely caused by differential attenuation. We will discuss this matter further in section 4.5.2. Similar to Case 2, quasi-nodes and quasi-antinodes existing in all regions in Figure 6c suggest that both the brash and frazil ice interfaces are strong reflectors of wave energy, which will be discussed in section 4.5.3.

4.5. Wave Energy Flux

4.5.1. Mean Attenuation

To investigate the overall energy modulation of waves interacting with ice, we integrate energy flux over all frequencies to remove the influence of nonlinear energy transfers between frequencies. As a result, the remaining mechanisms that can change the frequency-integrated energy flux are reflection and dissipation [*Masson and LeBlond*, 1989; *Meylan and Masson*, 2006]. Figure 8 shows the total energy flux plotted against propagation distance with a spatial resolution of 0.3 m for all three cases. For no-ice in Case 1, the mean energy flux remains constant but contains oscillations due to partially standing waves from the reflecting coastal structure. For pancake ice in Case 2, similar strong energy flux oscillations appear in the ice-free region ($Y >$ 36 m), indicative of reflected waves from the pancake ice interface with the open water. Once the waves enter the pancake ice ($Y <$ 36 m), total energy flux is rapidly attenuated. In this study, we employ a one-dimensional scattering theory to model an exponential energy decay with propagation distance energy decay in ice [*Wadhams*, 1986], i.e.,

$$E_f(x) = E_f(0)e^{-qx}. \tag{6}$$

In equation (6), x is the distance the waves have penetrated into the ice field; q is the energy attenuation rate; $E_f(x)$ is the energy of a wave group centered on frequency f, and $E_f(x=0)$ is the original energy entering the ice covered region. Note that the original model by *Wadams et al*. [1986] only considered energy by assuming a constant group velocity. In this study we include the group velocity observed in section 4.3 and extended to the energy flux instead of energy. By fitting the observations of the pancake ice within $Y <$ 36 m, the bulk attenuation rate is found to be -0.10 m^{-1}. For brash/frazil ice in Case 3, the energy flux within brash ice region (26 m $< Y <$ 35 m) is dominated by large oscillations with a slightly decreasing magnitude, suggesting that attenuation due to the brash ice is small compared to reflection from the brash-frazil interface. As the waves propagate through the frazil ice ($Y <$ 26 m), energy flux decays exponentially

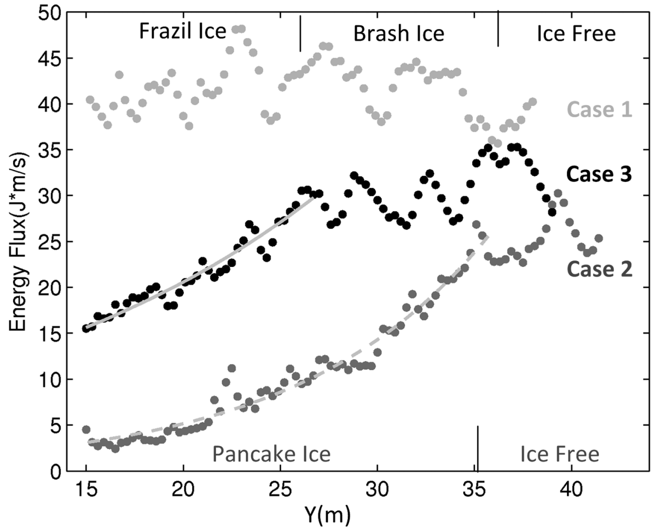

Figure 8. Total energy flux evolution along the cross-shore *Y* direction for Case 1 (●), Case 2 (●), and Case 3 (●). The dashed and solid gray lines correspond to the regression fit for pancake ice in Case 2 ($q=-0.10\ m^{-1}$) and frazil ice in Case 3 ($q=-0.055\ m^{-1}$), respectively.

with a fitting bulk attenuation rate q of $-0.055\ m^{-1}$. Small oscillations in energy flux are the indicative of the presence of weak reflected waves from the coastal structure.

4.5.2. Spectral Attenuation

Under a steady state condition, any change in energy flux over specified frequency bandwidth could be caused by either a nonlinear energy transfer across frequencies, reflection by due to the coastal structure/ice interface, or dissipation [*Perrie and Hu*, 1996; *Elgar et al.*, 1997]. In this study, we integrate the energy flux of pancake ice in Case 2 (Figure 6b) over three different frequency bands of equal width: 0.38–0.44 Hz (low), 0.44–0.50 Hz (middle), and 0.50–0.56 Hz (high), yielding the three distinct spectral evolutions over the cross-shore direction with a spatial resolution of 0.3 m in Figure 9a. Adjacent to the interface between ice-free and pancake ice (i.e., $Y \sim 36$ m), the three chosen bands of energy wave flux experience slight gradual increase, which may be owing to a nonlinear energy transfer caused by ice collisions [*Wadhams et al.*, 1988]. Inside the pancake ice (e.g., $Y < 35$ m), nonlinear energy transfers among the chosen frequency bands are considered negligible, since no frequency band experiences an increase/decrease in energy. Furthermore, wave energy decays considerably within the pancake ice field (for detailed discussion, see in section 4.5.3), reflective waves are deemed to be negligible. Therefore, changes in energy flux of the bandwidths are attributed to dissipation from ice. We fit the energy flux in each frequency band using equation (6) to obtain spectral attenuation. Energy flux within the high-frequency band attenuates the fastest with $q=-0.11\ m^{-1}$, followed by the middle frequency band with $q=-0.08\ m^{-1}$, with the low-frequency band being attenuated the slowest with $q=-0.06\ m^{-1}$. In other words, if irregular waves propagate through pancake ice, the higher-frequency waves are attenuated faster than the lower-frequency waves, yielding the

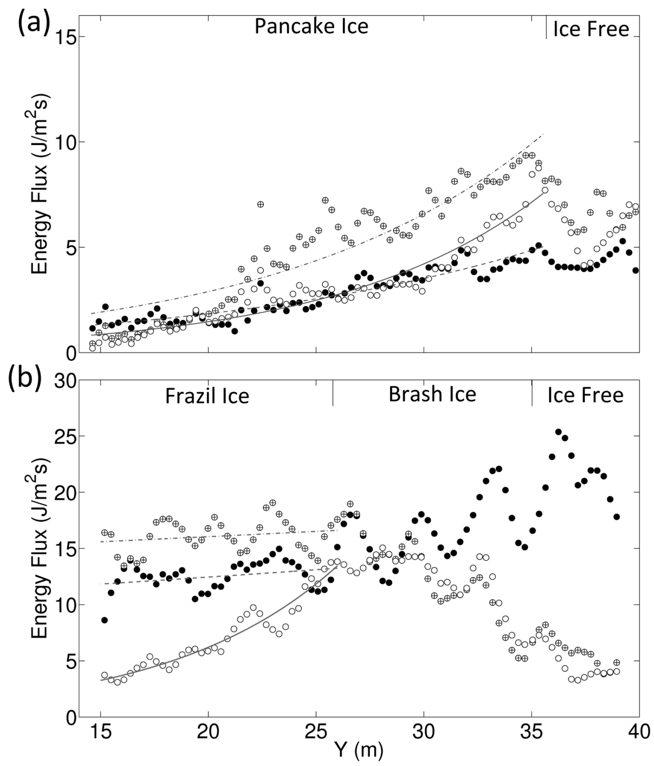

Figure 9. Spectral energy flux evolution along the cross-shore *Y* direction for (a) Case 2 with frequency bands corresponding to 0.38 to 0.44 Hz (●), 0.44 to 0.5 Hz (⊕), and 0.5 to 0.56 Hz (○) and (b) Case 3 with frequency bands of 0.49 to 0.53 Hz (●), 0.53 to 0.57 Hz (⊕), and 0.57 to 0.61 Hz (○). The lines in both (a) and (b) correspond to the best fit to equation (6) for each given frequency band.

mean frequency to decrease. This differential attenuation of higher frequencies is clearly observed in the 3-D water surface reconstructions of Figure 3. The wave crests deeper into the pancake ice become more elongated and uniform, indicating a higher attenuation of higher frequencies relative to lower frequencies. Differential attenuation through pancake ice was also observed by *Wadhams et al*. [1986, 1988] and *Hayes et al*. [2007] for lower-frequency waves ($f < 0.3$ Hz). Since each frequency band interacting with ice has a unique spectral attenuation rate q, the overall wave climate can be significantly altered by differential attenuation.

For brash/frazil ice in Case 3, three different frequency bands of equal width, 0.49–0.53 Hz (low), 0.53–0.57 Hz (middle), and 0.57–0.61 Hz (high), are centered on the dominant frequencies in each ice region. Figure 9b shows the three distinct spectral evolutions against cross-shore distance with a spatial resolution of 0.3 m. The low-frequency band begins with the largest amount of energy flux in the ice-free region which quickly decreases by 30% in the brash ice region. On the other hand, both the middle and high-frequency bands experience increasing energy flux of 278% and 288%, respectively, from the ice-free region to the brash ice region ($26\text{ m} < Y < 35\text{ m}$). The mechanism responsible for the shift in energy flux to higher frequencies in brash ice is most likely due to nonlinear energy transfer from the low-frequency band to the mid and high-frequency bands. As hypothesized by *Wadhams et al*. [1988], nonlinear energy transfer is possibly induced by floe-floe interactions between brash ice particles. Once waves propagate into the region dominated by frazil ice ($Y < 26$ m), the high-frequency wave band rapidly attenuates with a spectral attenuation rate of $q = -0.13\text{ m}^{-1}$. In contrast, the mid and low-frequency bands experience relatively slight to moderate attenuation rates of $q = -0.006\text{ m}^{-1}$ and $q = -0.013\text{ m}^{-1}$, respectively. Similar to the pancake ice in Case 2, this differential attenuation of higher frequencies versus lower frequencies causes the decrease in the mean frequency in frazil ice (see Figure 7), which supports the section 4.4. Interestingly, the results reported here are consistent with laboratory experiments of monochromatic waves in frazil ice conducted by *Newyear and Martin* [1997], in which attenuation rates increase with increasing wave frequencies and the magnitudes are on the same order as laboratory measurements performed by *Wang and Shen* [2010a] for waves of similar frequency interacting with frazil/pancake ice. Overall the characteristic of differential attenuation holds for frazil and pancake ices since both acts as viscous-like layers [*Keller*, 1998].

4.5.3. Reflection

Figure 10 shows the spatial distribution of reflection coefficients in the cross-shore direction. For no-ice in Case 1 (see Figure 10a), the reflection coefficient oscillates but the mean remains relatively constant along the propagation direction with a slight increase for $Y > 22$ m. In the field experiment, reflection coefficient measurements start approximately 2.6 wavelengths from the reflecting structure (15 m offshore with a dominant wavelength of $L = 5.8$ m), a distance for which the reflection coefficient observations of *Huang et al*. [2003] were fairly stable and under some wave conditions slightly increased with distance from the reflecting structure. Overall, the mean observed reflection coefficient value in the ice-free condition is $K = 0.40$, similar to the value of 0.45 that *Bechle and Wu* [2011] calculated for the same coastal structure using a spatial array of stereo imaging-derived virtual wave gauges.

For pancake ice in Case 2, as seen in Figure 10b, the reflection is larger in the ice-free region compared with the pancake ice region, where the dashed line is the interface $Y = 36$ m. Specifically in the ice-free region, the reflection coefficient is $K = 0.51$ close to the ice edge and decreases away from the ice edge down to $K = 0.28$ at the limit of the measurement area. This phenomenon was similarly observed in pancake and pack ice fields by *Wadhams et al*. [1986], who concluded that reflection coefficient is a strong function of the distance from the ice front. The observed reflection coefficients fall within the range observed by *Wadhams et al*. [1986] for much larger ocean waves ($0.16 < K < 0.36$). The strong reflection at the ice-free/pancake ice interface explains the large oscillations in energy flux occurring at $Y > 36$ m in Figure 8, discussed in section 4.5. Inside the pancake ice field ($Y < 36$ m), the main cause of reflected waves is the coastal wall structure. The average reflection coefficient of the coastal structure in pancake ice is $K = 0.22$, much smaller than $K = 0.40$ for no-ice in Case 1. This can be explained by wave attenuation by the pancake ice as the reflected waves from the coastal structure propagate back to the measurement area 15 m offshore. As a result reflected wave energy is smaller relative to that for no-ice in Case 1.

For brash/frazil ice in Case 3, Figure 10c shows the reflection coefficient is small in the frazil ice, large in the brash ice, and medium in the ice-free region. Inside the frazil ice field, the source of reflection is the coastal wall structure. The average reflection coefficient is $K = 0.14$, much smaller than observed in no ice in Case 1 owing to the attenuation of reflected waves through the frazil ice. Reflection from the frazil-brash ice is

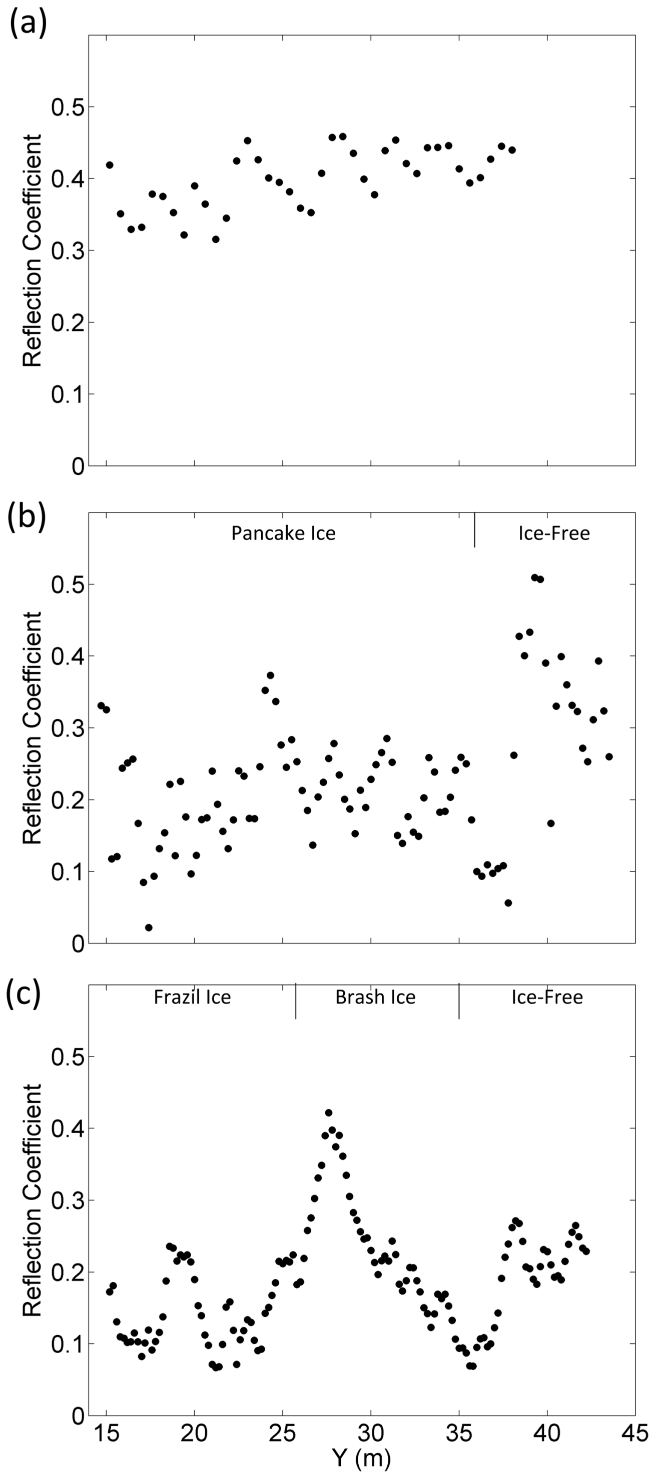

Figure 10. Reflection coefficient along the cross-shore *Y* direction for (a) Case 1, (b) Case 2, and (c) Case 3.

large ($K = 0.41$), and decreases in intensity away from the interface ($Y = 26$ m). This strong reflection, as well as the low attenuation of brash ice, is likely responsible for the large energy flux oscillations observed in the brash ice in Figure 8, discussed in section 4.5. Reflection from the brash ice interface with the ice-free region ($Y = 35$ m) is medium with $K = 0.24$, suggesting that the thin brash ice particles have less capacity to reflect energy than the thicker frazil and pancake ice layers. Also of note, magnitudes of these oscillations energy flux observed in Figure 8 are consistent with the reflection coefficients measured using incident and reflected wave energy.

5. Discussion

5.1. Brash Ice and Surface Wave Interactions

Field observations in brash-type ice indicate that wave attenuation through the ice field generally increases with frequency over the majority of the spectrum [*Squire and Moore*, 1980; *Wadhams et al*., 1988; *Frankenstein et al*., 2001]. However, a roll-over occurs at higher frequencies ($f > 0.1$ Hz) in which attenuation decreases with increasing frequency [*Wadhams et al*., 1988; *Frankenstein et al*., 2001; *Hayes et al*., 2007]. *Wadhams et al*. [1988] hypothesized that this roll-over effect may be caused by a nonlinear transfer of energy to higher frequencies as the result of floe-floe interactions, e.g., collisions and rafting. The high spatial resolution stereo imaging measurements made in this study provide evidence to support this hypothesis that nonlinear energy transfers to higher-frequency waves in brash ice are the likely source of the roll-over effect. As seen in the spatial frequency spectra of Figure 6c, the dominant wave frequency shifts from 0.51 Hz in the ice-free region to 0.59 Hz within one wavelength of entering the brash ice. This frequency shift agrees with the wavelength measurements shown in Figure 5f where peak wavelength decreases in the brash ice, independently indicating a shift to higher-frequency waves. Further evidence of an energy transfer to higher frequencies is found in the energy flux bands of Figure 9b, where upon entering the brash ice region ($Y < 35$ m), energy flux decreases in the lower frequency band while increasing in the two higher-frequency bands. This rapid observed increase in energy at the higher frequencies in brash ice is indicative of a nonlinear energy transfer [*Mei et al*., 2005; *Polnikov and Lavrenov*, 2007]. To investigate the plausibility of nonlinear wave interactions in the brash ice field, surface topography is examined for nonlinear indicators. Wave steepness is measured for individual waves from 10 successive 3-D water surface profiles along the offshore Y direction, similar to the profiles shown in Figure 5; wave steepness along these profiles is calculated as wave height H divided by wave length L, i.e., H/L. Mean wave steepness increases notably from $H/L = 0.08$ in the ice-free region to $H/L = 0.12$ after 7 m of propagation through brash ice; this 50% increase in steepness in the brash ice exceeds the increase expected from the observed wavelength decrease (Figure 5i). Based upon steepness criteria given by *Dean and Dalrymple* [1991], the waves transform from linear waves in the ice-free region into higher-order Stokes waves within the brash ice, further indicating that nonlinear mechanisms may be responsible for the frequency upshift in brash ice. Furthermore, the high brash ice concentration with small cohesion between particles and on-ice wind observed in this study create an environment favorable to floe-floe collisions [*Wadhams*, 2001]. Thus, the nonlinear energy transfer to higher frequencies observed in the brash ice supports the hypothesis of *Wadhams et al*. [1988] that nonlinear floe-floe interactions are the source of wave attenuation roll-over in brash-type ice.

5.2. Spatial Resolution and Wave Attenuation

Spatial attenuation of waves interacting with ice follows the scattering model (equation (6)) originally hypothesized by *Wadhams* [1986], where wave energy decays exponentially with propagation distance through ice. Nevertheless, observations of wave energy decay through ice have been limited to confirm the scattering model, owing to the difficulty of obtaining high spatial resolution measurements throughout wave interacting with ice environment. *Hayes et al*. [2007] observed an exponential decay of wave energy over a 9 km ice field from AUV measurements under the ice, though the accuracy of the attenuation calculations was admittedly compromised at low frequencies by the surge response of the AUV. In this study, stereo imaging provided high spatial resolution measurements of wave energy flux on a subwavelength scale to examine spatial wave energy attenuation in detail. Spatial wave energy flux profiles for the pancake and frazil ices revealed that attenuation in these viscous-type ices can be described by the exponential decay model for both the mean energy flux (Figure 8) and the bandwidth integrated energy flux (Figure 9). Fluctuations in energy flux from partially standing waves are evident in these energy flux profiles, further illustrating the importance of high spatial resolution measurements of wave energy flux. If observations with a low-resolution array of point-based wave sensors were made, an aliased representation of the spatial pattern of attenuation can easily occur. The high spatial resolution of energy flux measurements is more vividly illustrated in the brash ice in Case 3 (Figure 8, black circles), in which the energy flux is highly oscillatory due to strong reflected waves. The energy flux has a very weak decreasing trend, suggesting a relative small dissipation. If arbitrary point-based measurements are placed, one may encounter severe aliasing in this oscillatory standing wave pattern, leading to a misleading conclusion to the behavior of waves in brash ice. For example, a point measurement array spaced at 4 m would indicate either an energy flux increase or decrease depending on the position of the array. On the other hand, the subwavelength-scale resolution provided by stereo imaging revealed the complex and detailed spatial pattern of the energy flux to properly characterize the behavior of wave attenuation through ices.

5.3. Ice Types and Wave Reflection

Reflection of incident wave energy was observed for three types of ice interfaces. The reflection coefficients decrease away from the interface, consistent to those inferred from the point-based observations [*Wadhams et al*., 1986]. As reflected waves propagate in the opposite direction of the incident waves, they scatter and decay [*Huang et al*., 2003]. Reflection coefficients appear to decrease the fastest away from the frazil/brash ice interface (see Figure 10c). In contrast, the waves reflecting from pancake/ice-free (see Figure 10b) or brash/ice-free (see Figure 10c) interfaces into the ice-free water field endure less energy dissipation and scattering than the brash ice field. To quantify the impact of ice types on wave reflection, we fit the spatial distribution of observed reflection coefficients by an exponential model

$$K=\alpha\left(\frac{d}{L}\right)^{\beta}, \tag{7}$$

where L is wavelength, d is the distance from the reflector, α and β are a constant and decay rate, respectively [*Huang et al.*, 2005]. Both the interfaces of pancake/ice-free ($\alpha = 0.28$, $\beta = -0.15$) and brash/ice-free ($\alpha = 0.19$, $\beta = -0.10$) exhibit similar decay rates β, whereas the interface of frazil-brash ($\alpha = 0.16$, $\beta = -0.49$) has a larger decay rate. In other words, the reflected waves through the brash ice are scattered or dissipated at a much higher rate than through the ice-free open water. Meanwhile it is of notice that the attenuation of incident waves through the brash ice is negligible (Figure 9), suggesting that wave scattering induced by the floe interactions with brash ice particles is likely the cause of this increased rate of reflection coefficient decay. Therefore, the distance at which reflection coefficient reaches equilibrium is expected to be shorter through ice ($<$2 wavelengths) than through an ice-free condition ($\sim$4 wavelengths).

6. Summary and Conclusions

In this study, the Automated Trinocular Stereo Imaging System (ATSIS) was improved with a phase-only correlation (POC) algorithm and a parallel computation algorithm to reconstruct the 3-D water surface in the presence of ice. ATSIS was used to remotely measure surface waves interacting with three different types of ice: pancake, frazil, and brash ices. High temporal and spatial resolution wave measurements made possible by ATSIS were used to characterize the wave propagation through ice in terms of wavelength, speed, frequency, and energy. Results show that the mean frequency(wavelength) in pancake and frazil ice decreases(increases) due to differential attenuation, as higher-frequency waves attenuate faster than lower-frequency waves. In contrast, for brash ice, energy is rapidly transferred from a lower-frequency band to a higher-frequency band over a distance of approximately one wavelength. This frequency upshift is believed to be the result of a nonlinear energy transfer caused by small cohesion between brash ice particles creating favorable conditions for collisions and floe-floe interactions.

Spatial observations of wave energy flux revealed differences in the attenuation and reflection behavior of the ice types. Total wave energy flux was observed to decrease in both pancake and frazil ice, whereas in brash ice energy flux remained relatively constant. The minimal attenuation in brash ice is attributed to the thin ice layer thickness ($\sim$5 cm) compared to the much thicker frazil and pancake ice fields ($\sim$25 cm). Spatial energy flux profiles reveal that wave reflection occurs at the boundary of each ice layer, with reflection strongest at the pancake/ice-free and frazil/brash interfaces and weakest at the brash/ice-free interface. Reflection coefficient decreases exponentially with distance from the reflecting interface. The decay rate is much greater for reflected waves propagating through another ice field rather than into an ice-free condition, illustrating the scattering effect the ice has on reflected waves. These observations measured by ATSIS demonstrate the spatially variable nature of waves propagating through ice, indicating the necessity of high spatial and temporal resolution measurements to properly characterize the behavior of waves interacting with ice.

Acknowledgments
This research was partly supported by the University of Wisconsin-Sea Grant Wisconsin under the grant award NA10OAR4170070 and Great Lakes Consortium for Ocean and Human Health (OHH) under the grant contract 113405548. In addition, funding support for the first author by the University of Wisconsin-Hilldale Fellowship and second author by the National Science Foundation Graduate Research Fellowship is acknowledged. The authors specifically thank Tom Baldock at the University of Queensland for his kindness to share the Matlab codes for separating incident and reflective waves, published in *Baldock and Simmonds* [1999]. We also thank John Magnuson for his insight on ice phonology in lakes. Last but not least, we truly acknowledge the support and comments provided by two anonymous reviewers.

References

Alpers, W. R., D. B. Ross, and C. L. Rufenach (1981), On the detectability of ocean surface waves by real and synthetic aperture radar, *J. Geophys. Res.*, *86*(C7), 6481–6498.
Baldock, T. E., and D. J. Simmonds (1999), Separation of incident and reflected waves over sloping bathymetry, *Coastal Eng.*, *38*(30), 167–176, doi:10.1016/S0378-3839(99)00046-0.
Banner, M. L., I. S. F. Jones, and J. C. Trinder (1989), Wavenumber spectra of short gravity waves, *J. Fluid Mech.*, *198*, 321–344.
Barnes, P. W., E. W. Kempema, E. Reimnitz, and M. McCormick (1994), The influence of ice on southern Lake Michigan coastal erosion, *J. Great Lakes Res.*, *20*(1), 179–195.
Bechle, A. J., and C. H. Wu (2011), Virtual wave gauges based upon stereo imaging for measuring surface wave characteristics, *Coastal Eng.*, *58*(4), 305–316, doi:10.1016/j.coastaleng.2010.11.003.
Benetazzo, A. (2006), Measurements of short water waves using stereo matched image sequences, *Coastal Eng.*, *53*(12), 1013–1032, doi:10.1016/j.coastaleng.2006.06.012.
Benetazzo, A., F. Fedele, G. Gallego, P.-C. Shih, and A. Yezzi (2012), Offshore stereo measurements of gravity waves, *Coastal Eng.*, *64*, 127–138, doi:10.1016/j.coastaleng.2012.01.007.
Brown, L. G. (1992), A survey of image registration techniques, *Comput. Surv.*, *24*(4), 325–376.
Cote, L. J., J. O. Davis, W. Marks, R. J. McGough, E. Mehr, W. J. Pierson, J. F. Ropek, G. Stephenson, and R. C. Vetter (1960), The directional spectrum of wind generated sea as determined from data obtained by the stereo wave observation project, *Meterol. Pap.*, *2*(6), 395–400.
Dean, R. G., and R. A. Dalrymple (1991), *Water Wave Mechanics for Engineers and Scientists*, World Sci., Singapore.
de Vries, S., D. Hill, M. A. de Schipper, and M. J. F. Stive (2011), Remote sensing of surf zone waves using stereo imaging, *Coastal Eng.*, *58*(3), 239–250, doi:10.1016/j.coastaleng.2010.10.004.
Elgar, S., R. T. Guza, B. Raubenheimer, T. H. C. Herbers, and E. L. Gallagher (1997), Spectral evolution of shoaling and breaking waves on a barred beach, *J. Geophys. Res.*, *102*(C7), 15,797–15,805, doi:10.1029/97JC01010.
Forbes, D. L., and R. B. Taylor (1994), Ice in the shore zone and the geomorphology of cold coasts, *Prog. Phys. Geogr.*, *18*(1), 59–96, doi:10.1177/030913339401800104.
Foroosh, F., J. B. Zerubia, and M. Berthod (2002), Extension of phase correlation to subpixel registration, *IEEE Trans. Image Process.*, *11*(3), 188–200, doi:10.1109/83.988953.

Foschi, R., M. Isaacson, N. Allyn, and S. Yee (1996), Combined wave-iceberg loading on offshore structures, *Can. J. Civil Eng.*, *23*(5), 1099–1110, doi:10.1139/l96-917.

Fox, C., and T. G. Haskell (2001), Ocean wave speed in the Antarctic marginal ice zone, *Ann. Glaciol.*, *33*, 350–354, doi:10.3189/172756401781818941.

Fox, C., and V. A. Squire (1990), Reflection and transmission characteristics at the edge of shore fast sea ice, *J. Geophys. Res.*, *95*(C7), 11,629–11,639, doi:10.1029/JC095iC07p11629.

Fox, C., and V. A. Squire (1991), Strain in shore fast ice due to incoming ocean waves and swell, *J. Geophys. Res.*, *96*(C3), 4531–4547, doi:10.1029/90JC02270.

Frankenstein, S., S. Loset, and H. H. Shen (2001), Wave-ice interactions in Barents Sea Marginal Ice Zone, *J. Cold Reg. Eng.*, *15*(2), 91–102, doi:10.1061/(ASCE)0887-381X(2001)15:2(91).

Frigaard, P., and M. Brorsen (1995), A time-domain method for separating incident and reflected irregular waves, *Coastal Eng.*, *24*(3–4), 205–215, doi:10.1016/0378-3839(94)00035-V.

Frigaard, P., J. Helm-Peterson, G. Klopman, C. T. Stansberg, and M. Benoit (1997), IAHR list of sea state parameters: An update for multidirectional waves, in *Proceedings of the Twenty-Seventh IAHR Congress*, pp. 15–19, Can. Gov. Publ., The International Association for Hydro-Environment Engineering and Research (IAHR).

Ghobrial, T. R., M. R. Loewen, and F. E. Hicks (2013), Characterizing suspended frazil ice in rivers using upward looking sonars, *Cold Reg. Sci. Technol.*, *86*, 113–126, doi:10.1016/j.coldresions.2012.10.002.

Goodman, L., E. R. Levine, and Z. K. Wang (2010), Subsurface observations of surface waves from an autonomous underwater vehicle, *IEEE J. Oceanic Eng.*, *35*(4), 779–784 doi:10.1109/JOE.2010.2060551.

Hayes, D., A. Jenkins, and S. McPhal (2007), Autonomous underwater vehicle measurements of surface wave decay and directional spectra in the marginal sea ice zone, *J. Phys. Oceanogr.*, *37*, 71–83, doi:10.1175/JPO2979.1.

Holland, K. T., R. A. Holman, T. C. Lippmann, J. Stanley, and N. Plant (1997), Practical use of video imagery in nearshore oceanographic field studies, *IEEE J. Oceanic Eng.*, *22*(1), 81–92, doi:10.1109/48.557542.

Holthuijsen, L. H. (1983), Observations of the directional distribution of ocean-wave energy in fetch-limited conditions, *J. Phys. Oceanogr.*, *13*(2), 191–207, doi:10.1175/1520-0485(1983)013<0191:OOTDDO>2.0.CO;2.

Holthuijsen, L. H. (2007), *Waves in Coastal and Oceanic Waters*, 404 pp., Cambridge Univ. Press, N. Y.

Huang, W. P., C. R. Chou, and J. Yim (2003), Experiments on the reflection coefficients of a detached breakwater in a directional wave field, *Coastal Eng.*, *47*, 367–379.

Huang, W. P., C. R. Chou, and J. Yim (2005), On reflection and diffraction due to a detached breakwater, *Ocean Eng.*, *32*, 1762–1779.

Ibrahim, R. A., N. G. Chalhoub, and J. Falzarano (2007), Interaction of ships and ocean structures with ice loads and stochastic ocean waves, *Appl. Mech. Rev.*, *60*(5), 246–290, doi:10.1115/1.2777172.

Jähne, B., J. Klinke, and S. Waas (1994), Imaging of short ocean wind waves: A critical theoretical review, *J. Opt. Soc. Am.*, *11*(8), 2197–2209, doi:10.1364/JOSAA.11.002197.

Keller, J. B. (1998), Gravity waves on ice-covered water, *J. Geophys. Res.*, *103*(C4), 7663–7670.

Kohout, A. L., M. H. Meylan, and D. R. Plew (2011), Wave attenuation in a marginal ice zone due to the bottom roughness of ice floes, *Ann. Glaciol.*, *52*, 118–122.

Masson, D., and P. H. LeBlond (1989), Spectral evolution of wind-generated surface gravity-waves in a dispersed ice field, *J. Fluid Mech.*, *202*, 43–81, doi:10.1017/S0022112089001096.

Mei, C. C., M. Stiassnie, and D. K. P. Yue (2005), *Theory and Applications of Ocean Surface Waves Part 2: Nonlinear Aspects*, World Sci., Toh Tuck Link, Singapore.

Meylan, M. H., and D. Masson (2006), A linear Boltzmann equation to model wave scattering in the marginal ice zone, *Ocean Modell.*, *11*, 417–427, doi:10.1016/j.ocemod.2004.12.008.

Meylan, M. H., and V. A. Squire (1996), Response of circular ice floe to ocean waves, *J. Geophys. Res.*, *101*(C4), 8869–8884.

Newyear, K., and S. Martin (1997), A comparison of theory and laboratory measurements of wave propagation and attenuation in grease ice, *J. Geophys. Res.*, *102*(C11), 25,091–25,100.

Perrie, W., and Y. Hu (1996), Air-ice-ocean momentum exchange. Part 1: Energy transfer between waves and ice floes, *J. Phys. Oceanogr.*, *26*(9), 1705–1720, doi:10.1175/1520-0485(1996)026<1705:AMEPTB>2.0.CO;2.

Polnikov, V. G., and I. V. Lavrenov (2007), Calculation of the nonlinear energy transfer through the wave spectrum at the sea surface covered with broken ice, *Oceanology*, *47*(3), 334–343.

Schumacher, A. (1939), Stereophotogrammetrische Wellenaufnahmen, in *Wiss. Ergeb. Dtsch. Atlant. Exped. Forschungs Vermessung. "Meteor"* 1925–1927, Ozeanographische Sonderuntersuchungen, Erste Lieferung, Berlin.

Shemdin, O. H., H. M. Tran, and S. C. Wu (1988), Directional measurement of short ocean waves with stereophotography, *J. Geophys. Res.*, *93*(C11), 13,891–13,901.

Shen, H. H., S. F. Ackley, and M. A. Hopkins (2001), A conceptual model for pancake-ice formation in a wave field, *Ann. Glaciol.*, *33*, 361–367.

Shen, H. H., S. F. Ackley, and Y. Yuan (2004), Limiting diameter of pancake ice, *J. Geophys. Res.*, *109*, C12035, doi:10.1029/2003JC002123.

Squire, V. A. (2007), Of ocean waves and sea-ice revisited, *Cold Reg. Sci. Technol.*, *49*(2), 110–133, doi:10.1016/j.coldregions.2007.04.007.

Squire, V. A. (2011), Past, present and impendent hydroelastic challenges in the polar and subpolar seas, *Philos. Trans. R. Soc. A*, *369*, 2813–2831, doi:10.1098/rsta.2011.0093.

Squire, V. A., and S. C. Moore (1980), Direct measurement of the attenuation of ocean waves by pack ice, *Nature*, *283*(5745), 365–368.

Squire, V. A., J. P. Dugan, P. Wadhams, P. J. Rottier, and A. K. Liu (1995), Of ocean waves and sea ice, *Ann. Rev. Fluid Mech.*, *27*, 115–168, doi:10.1146/annurev.fluid.27.1.115.

Squire, V. A., G. L. Vaughan, and L. G. Bennetts (2009), Ocean surface wave evolvement in the Arctic Basin, *Geophys. Res. Lett.*, *36*, L22502, doi:10.1029/2009GL040676.

Sugimori, Y. (1975), A study of the application of the holographic method to the determination of the directional spectrum of ocean waves, *Deep Sea Res. Oceanogr. Abstr.*, *22*, 339–350.

Wadhams, P. (1986), The seasonal ice zone, in *The Geophysics of Sea Ice*, edited by N. Untersteiner, pp. 825–991, Springer, Plenum, N. Y.

Wadhams, P. (2001), *Ice in the Ocean*, Gordon and Breach, Amsterdam.

Wadhams, P., V. A. Squire, J. A. Ewing, and R. W. Pascal (1986), The effect of the marginal ice-zone on the directional wave spectrum of the ocean, *J. Phys. Oceanogr.*, *16*(2), 358–376, doi:10.1175/1520-0485(1986)016<0358:TEOTMI>2.0.CO;2.

Wadhams, P., V. A. Squire, D. J. Goodman, A. M. Cowan, and S. C. Moore (1988), The attenuation rates of ocean waves in the marginal ice zone, *J. Geophys. Res.*, *93*(C6), 6799–6818.

Wadhams, P., F. E. Parmiggiani, G. de Carolis, D. Desiderio, and M. J. Doble (2004), SAR imaging of wave dispersion in Antarctic pancake ice and its use in measuring ice thickness, *Geophys. Res. Lett.*, *31*, L15305, doi:10.1029/2004GL020340.
Wanek, J. M., and C. H. Wu (2006), Automated Trinocular stereo imaging system for three-dimensional surface wave measurements, *Ocean Eng.*, *33*(5–6), 723–747, doi:10.1016/j.oceaneng.2005.05.006.
Wang, R., and H. H. Shen (2010a), Experimental study on surface wave propagating through a grease-pancake ice mixture, *Cold Reg. Sci. Technol.*, *61*(2–3), 90–96, doi:10.1016/j.coldregions.2010.01.011.
Wang, R., and H. H. Shen (2010b), Gravity waves propagating into an ice-covered ocean: A viscoelastic model, *J. Geophys. Res.*, *115*, C06024, doi:10.1029/2009JC005591.
Wang, R., and H. H. Shen (2011), A continuum model for wave propagation in ice-covered oceans: An approximate solution, *Ocean Modell.*, *38*, 244–250, doi:10.1016/j.ocemod.2011.04.002.
Wang, R., and H. H. Shen (2013), On developing a continuum model for wave propagation in ice covered seas, in *Coastal Hazards*, edited by W. Huang, K.-H. Wang, and J. Cheng, pp. 24–32, doi:10.1061/9780784412664.003.
Weber, J. E. (1987), Wave attenuation and wave drift in the marginal ice zone, *J. Phys. Oceanogr.*, *17*, 2351–2361.
Weitz, M., and J. B. Keller (1950), Reflection of water waves from floating ice in water of finite depth, *Commun. Pure Appl. Math.*, *3*, 305–318, doi:10.1002/cpa.3160030306.
Wolf, P., and B. DeWitt (2000), *Elements of Photogrammetry: With Applications in GIS*, 608 pp., McGraw-Hill, Boston, Mass.
Zhao, X., and H. H. Shen (2013), Ocean wave transmissions and reflection between two connecting viscoelastic ice covers: An approximate solution, *Ocean Modell. 71*, 102–113.